AIAA JOURNAL
Vol. 45, No. 7, July 2007

Optimization of Mass Bleed for Base-Drag Reduction

Young-Ki Lee*
Poongsan Company, Nonsan, Chungnam 320-822, Republic of Korea
Heuy-Dong Kim†
Andong National University, Andong, Gyeongbuk 760-749, Republic of Korea
and
Srinivasan Raghunathan‡
Queen's University of Belfast, Belfast, BT9 5AG Northern Ireland, United Kingdom

DOI: 10.2514/1.23085

Efficient mass-bleed conditions to minimize base drag are examined in consideration of various base-to-orifice-exit area ratios for a body of revolution in the Mach 2.47 freestream. Axisymmetric, compressible, mass-averaged Navier–Stokes equations are solved using the standard k-ω turbulence model, a fully implicit finite volume scheme, and a second-order upwind scheme. Base flow characteristics are explained regarding the base configuration as well as the injection parameter, which is defined as the mass flow rate of the bleed jet nondimensionalized by the product of the base area and freestream mass flux. The results obtained through the present study show that for a smaller base area, the optimum mass-bleed condition leading to minimum base drag occurs at relatively larger mass bleed, and a larger orifice exit can offer better drag control.

Nomenclature

A	=	area
a	=	sound speed
D	=	diameter
I	=	injection parameter
k	=	turbulent kinetic energy
M	=	Mach number
$\dot{m}$	=	mass flow rate
p	=	pressure
R	=	radius
Re_{unit}	=	unit Reynolds number
r	=	radial distance
S	=	stagnation point
T	=	temperature
U	=	mean velocity
x	=	axial distance
ω	=	specific dissipation rate

Subscripts

b	=	base
e	=	orifice exit
f	=	forward
j	=	bleed jet
r	=	rear
ref	=	reference
0	=	total state
∞	=	freestream

Presented as Paper 1046 at the 43rd AIAA Aerospace Sciences Meeting and Exhibit, Reno, NV, 10–13 January 2005; received 9 February 2006; revision received 13 July 2006; accepted for publication 7 January 2007.

*Manager, Technical Research Laboratory; yklee@poongsan.co.kr.
†Professor, School of Mechanical Engineering; kimhd@andong.ac.kr. Member AIAA.
‡Professor, School of Aeronautical Engineering, Bombardier Aerospace—Royal Academy Chair; s.raghunathan@qub.ac.uk. Associate Fellow AIAA.

Introduction

IN HIGH-SPEED flight, aerodynamic bodies such as projectiles, powered missiles, and rockets generally undergo severe deterioration of flight performance from drag. For these kinds of flight bodies, especially, pressure drag generated due to low base pressure almost always rules total drag. For instance, in the case of a typical projectile at Mach 0.9 without a drag-control technique, base drag takes a major portion: up to 50% of total drag [1]. Base drag should, therefore, be considered separately from other pressure-drag components. For this reason, the minimization of base drag has been an important issue to date, and considerable effort has been made to find suitable techniques for obtaining low-base-drag shell design.

A number of experimental and computational studies have reported that base-drag reduction can be achieved by afterbody boattailing [2], base bleed or base burning [3,4], some vortex suppression devices [5], and their combinations [6]. Such active or passive flow control techniques, basically manipulate or alter the near-wake flowfield for an increase in base pressure and consequently reduce base drag. However, these techniques were applied in somewhat empirical manners to date, due to a lack of understanding of viscous–inviscid flow interaction between a near-wake flow and the freestream.

Figure 1 shows the schematic diagram of a supersonic base flow over the afterbody model under consideration in the present computation. The supersonic freestream expands through a Prandtl–Meyer expansion fan generated at the base corner, and the wall boundary layer developed toward the base is separated at the corner and recompressed by compression waves at a certain downstream region. The interaction between two distinct flows inside and outside the separation leads to a free shear layer along the boundary of the flows and recirculating flows inside the separation. In the presence of low mass bleed into the separated region, such flow features can be significantly changed, depending on the mass flow rate of the bleed jet for a given freestream Mach number and afterbody geometry [7].

According to a computational study conducted by Sahu and Nietubicz [1] using thin-layer Navier–Stokes equations at transonic speeds of Mach 0.9 to 1.2, the use of mass bleed can reduce base drag by 40–80%. With excessive mass bleed, however, there can be an adverse effect, which base pressure rather decreases. The experimental results obtained by Bourdon and Dutton [8] showed that an optimum condition giving a maximum base pressure was observed at a certain mass flow rate of the bleed jet for a given freestream Mach number of about 2.5. This important feature should

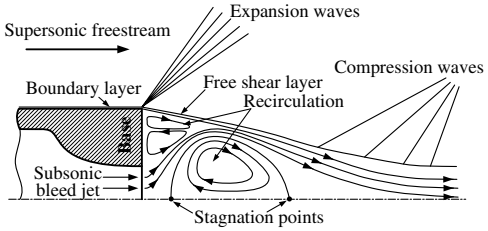

Fig. 1 Supersonic base flow with mass bleed.

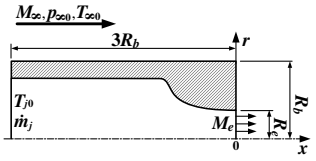

Fig. 2 Afterbody model.

have been validated with computational results to be considered in practical aerodynamic design with reliability.

In the present study, a compressible base flow in a supersonic freestream at Mach 2.47 was numerically investigated. Computations were conducted using axisymmetric mass-averaged Navier–Stokes equations with a fully implicit finite volume scheme and the standard k-ω turbulence model [9]. Some of results are validated with experimental data [10] and are also supported by detailed flow visualization to provide a better understanding of the physics of base flow controlled by the bleed jet. To obtain various characteristics of base flow, the mass flow rate of the bleed jet and the base-to-orifice-exit area ratio are changed for either fixed-model or orifice dimensions.

Computational Analysis

Testing Model

Figure 2 shows the afterbody model used in the present computational fluid dynamics (CFD) analysis. The mass flow rate of the bleed jet, $\dot{m}_j$, and the Mach number at the orifice exit, M_e, are calculated by isentropic relations corresponding to the mass bleed under consideration. Regarding model dimensions, the radii of the model and orifice exit are given as R_b and R_e, respectively. For reducing the computational time and resource of base flow simulation, it is appropriate to consider only part of the afterbody in computation so that the testing model has a length of $3R_{b,\text{ref}}$ taken from the origin, which is the center of the orifice exit. For the given afterbody length, a predefined velocity profile is considered at the inflow boundary to satisfy the boundary-layer thickness on the afterbody just before separation of about 3.2 mm, known experimentally [11]. The comparison of computed and measured boundary-layer profiles obtained 1 mm upstream of the base corner is given in Fig. 3.

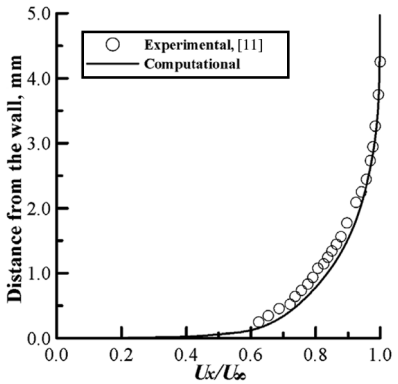

Fig. 3 Boundary-layer velocity profiles near the base corner.

Table 1 Details of the reference model

M_∞	2.47	Re_{unit}	46×10^6 m^{-1}
$p_{\infty 0}$	470 kPa	T_{j0}	293 K
p_∞	28.8 kPa	$R_{b,\text{ref}}$	31.75 mm
$T_{\infty 0}$	300 K	$R_{e,\text{ref}}$	12.70 mm

The details of the model geometry and properties chosen to specify flow conditions are shown in Table 1, in which Re_{unit} is the Reynolds number per unit length. The radii of base and orifice exit of the reference model, which is taken from [10] for validation, are defined as $R_{b,\text{ref}}$ and $R_{e,\text{ref}}$, respectively. With the values given in the table, the area ratio A_b/A_e for the reference model is 6.25. To examine the effect of the base-to-orifice-exit area ratio on base flow physics, the Reynolds number is changed for the given $R_{b,\text{ref}}$, or vice versa.

Numerical Methods

The present CFD study adopted a commercial computational code, FLUENT 6 [12], to simulate complex flow interaction between a supersonic freestream and a subsonic wake flow. Axisymmetric, compressible, mass-averaged Navier–Stokes equations were solved to investigate various characteristics of flowfield around a cylindrical afterbody, depending on mass bleed generated through an orifice installed in the model. For better convergence and accurate solutions, the solution procedure includes the preconditioning treatment [13], which allows the propagation of acoustic waves in the system to be singled out. The details of the governing equations and the preconditioning treatment can be referred to in [14].

The governing equations are discretized spatially using a fully implicit finite volume scheme, in which the physical domain is subdivided into numerical cells and the integral equations are applied to each cell. The flowfield is represented by associating a distinct value of the discretized solution vector with each control volume, which is then used to evaluate the fluxes at the cell faces. The solution vector is computed using a multidimensional linear reconstruction approach [15], which enables higher-order accuracy to be achieved at the cell faces through a Taylor series expansion of the cell-averaged solution vector. The use of a second-order upwind scheme makes it feasible to capture the location and structure of wave systems and shear flow, but only with fine computational grids in those regions. With respect to temporal discretization, an explicit multistage time-stepping scheme [16] is used to discretize the time derivatives in the governing equations. Then it is assumed that time marching proceeds until a steady-state solution is reached.

To obtain accurate solutions for the base flow including separation regions, wakes, strong free shear layers, and wave systems, suitable turbulence modeling is also indispensable. Preliminary computations were carried out for several turbulence models with and without wall functions. In the present numerical analysis, as a consequence, the standard k-ω turbulence model was selected. Some of results obtained through the preliminary tests are presented in the Results and Discussion section. The k-ω turbulence model adopted in this study is built based on the Wilcox k-ω model [9], modified for proper predictions of low-Reynolds-number effects, compressibility, and shear flow. Especially, the compressibility effect is incorporated in the expression of the dissipation of ω as a function of the turbulent Mach number $M_t[=(k/a^2)^{0.5}]$ [17]. The model has an ability to predict a spreading rate of free shear flow that is in close agreement with measurements for far wakes, mixing layers, and all types of jet flows, and it is therefore considered as a suitable turbulence model to simulate the supersonic base flow with mass bleed under consideration.

Computational Grids and Analysis

Figure 4 shows a grid layout near the afterbody model and brief information of the computational domain with boundary conditions used in the current CFD analysis. To ensure freestream conditions and thus to obtain better convergence, the computational domain is set up with dimensions of $50D_b$, where D_b is the model diameter,

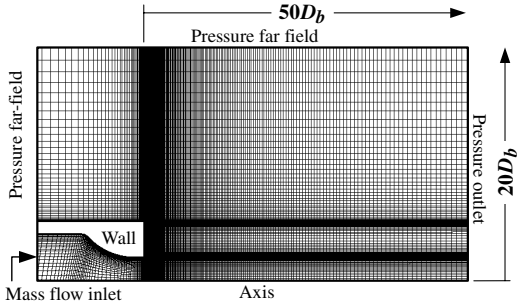

Fig. 4 Computational grids.

downwards from the base and $20D_b$ upwards from the model axis. Grids were clustered in the regions with a large pressure gradient, such as near model surfaces and downstream of the base, in which the separation of a wall boundary layer and complicated wave systems are expected to exist. Deliberating these points, it was found that about 50,000 nodes are required to get grid-independent solutions with the computational domain.

Freestream boundaries are identified with a combination of the pressure far-field and pressure outlet conditions, as shown in the figure. For this domain, preliminary tests showed that better convergence could be achieved using the combination rather than the use of the pressure far-field condition at all outer boundaries. To specify the freestream condition, the Mach number and static properties are applied to the boundaries, and a freestream turbulent intensity of 1% is used because such a low value was estimated in the experiment [11].

A circular-air-jet flow is generated through an orifice into the near-wake region behind the model base. For offering various characteristics of mass bleed, the mass flow rate of the bleed jet ($\dot{m}_j$) applied to the mass flow inlet boundary is changed corresponding to the injection parameter, given as follows:

$$I = \frac{\dot{m}_j}{A_b \rho_\infty U_\infty} \tag{1}$$

where A_b is the base area, and ρ_∞ and U_∞ are the density and velocity of the freestream. With a specified $\dot{m}_j$, the total temperature and static pressure are given at the inlet boundary. Adiabatic and no-slip conditions are applied to the wall boundaries, and an axis boundary condition is applied to the domain axis. The properties used for the boundary conditions mentioned are given in Table 1.

Regarding testing conditions, I is changed from 0.004 to 0.032 with fixed freestream conditions for each afterbody geometry tested. Base configurations are decided by a change in ether the base area or orifice exit area. The area ratios A_b/A_e, based on the reference value of R_b or R_e given in Table 1, are varied from 1.56 to 100. With a proper grid size and computational domain obtained through preliminary tests, solutions were basically considered converged when the residuals of mass, momentum, and energy equations dropped to 1.0×10^{-4}. The mass imbalance was also checked for

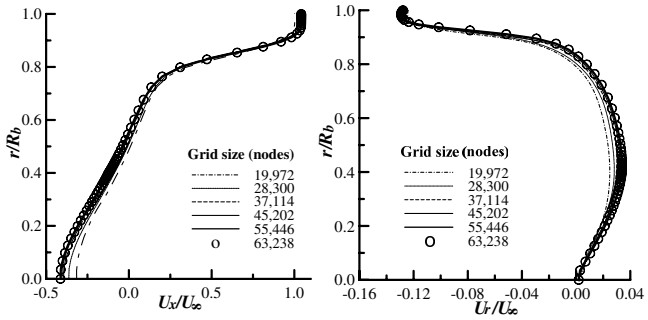

a) Axial velocity profiles at x/R_b= 1.0 b) Radial velocity profiles at x/R_b= 0.5

Fig. 5 Grid-dependence on the solution ($R_e = 12.7$ mm, $A_b/A_e = 6.25$, and $I = 0.0038$).

Table 2 Base pressure for $R_e = 12.7$ mm, $A_b/A_e = 6.25$, and $I = 0.0038$.

Turbulence model		p_b/p_∞
Standard k-ω		0.602
RNG k-ε	SWF	0.569
	NWF	0.572
RSM	SWF	0.571
	NWF	0.580
Experimental [10]		0.592

flow inlet and outlet boundaries, and the additional convergence criterion is satisfied because it is less than ±0.01% of the net incoming mass.

Results and Discussion

For $R_e = 12.7$ mm, $A_b/A_e = 6.25$, and $I = 0.0038$, Fig. 5 shows typical results of grid-fineness tests, given as axial velocity profiles at $x/R_b = 1.0$ and radial velocity profiles at $x/R_b = 0.5$ for several grid sizes. The velocity profiles were computed using the standard k-ω turbulence model. The radial distance and the axial and radial mean velocities U_x and U_r are normalized by R_b and U_∞, respectively. The grid size was tested in the range of about 20,000 to 63,500 nodes. In the figures, with an increase in grid size, the axial velocity changes noticeably inside the back flow region near the axis ($r/R_b = 0.0$) and the radial velocity does so behind the base, where the bleed jet interacts directly with the wake flow. Because the grid sizes more than 45,202 nodes yield no apparent change in the profile, it can be considered that 45,202 nodes are enough to obtain grid-independent solutions for the given value of I. For larger I values, in this approach, it was found that about 50,000 nodes can be used for the simulation of all base flows under consideration.

With a proper grid size obtained through the approach mentioned earlier, several turbulence models and wall functions were tested at $I = 0.0038$, and the results on the base pressure p_b, normalized by p_∞, are given in Table 2. In comparison with a measured value taken from [10], it is considered that the standard k-ω turbulence model, integrated all the way to the wall, can provide the most accurate prediction of base pressure. The results also indicate that the effect of wall functions applied to the renormalization group (RNG) k-ε and the Reynolds stress model (RSM) on the base-pressure prediction is insignificant for the base configurations and testing conditions used in the present computation. In the table, SWF and NWF denote the standard wall function and nonequilibrium wall function, respectively.

Figure 6 presents mean velocity vectors near the base, with and without base bleed, for $R_e = 12.7$ mm. In the figures, the axial and

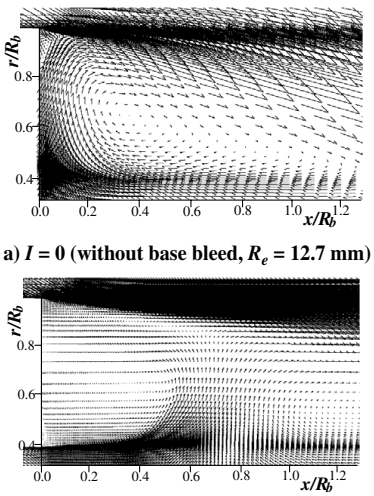

a) I = 0 (without base bleed, R_e = 12.7 mm)

b) I = 0.0113 (R_e = 12.7 mm and A_b/A_e= 6.25)

Fig. 6 Velocity vectors near the base.

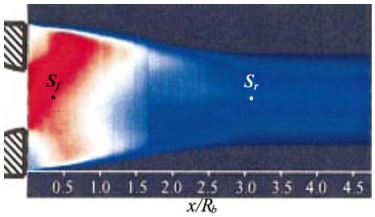

a) I= 0.0038

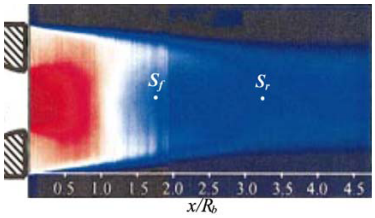

b) I= 0.0113

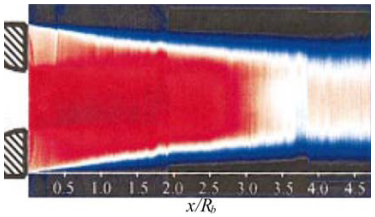

c) I= 0.0226

Fig. 7 Experimental visualization with average acetone laser-induced fluorescence signal [8].

radial distances are normalized by R_b. Without base bleed (the whole base region was treated as a wall), large and strong recirculating flows are observed behind the base. For typical flight bodies, total drag rises mainly due to a decrease in base pressure depending on such separation, which forms a wake region. As mass is injected into the separated region ($I = 0.0113$), the recirculation near the model base becomes weakened significantly.

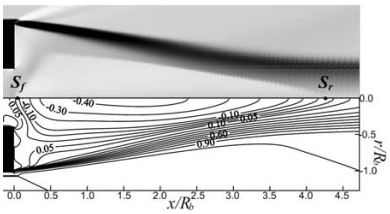

a) I= 0.0038

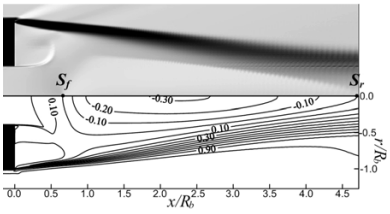

b) I= 0.0113

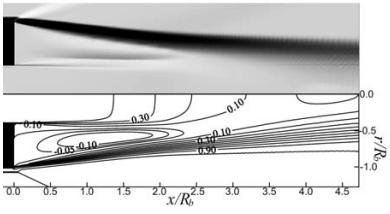

c) I= 0.0226

Fig. 8 Computed images based on density gradients and U_x/U_∞ contours.

Base flows visualized computationally and experimentally are compared through Figs. 7 and 8 to help understand the influence of the injection parameter on the flow structure. The experimental visualization presented in Fig. 7 is taken from [8]. The images were obtained using an acetone planar-laser-induced-fluorescence (PLIF) technique. The detailed description of the technique can be referred to in the reference. In Fig. 8, the computed images (upper halves) are developed by density gradients, and these are given with corresponding axial velocity contours valued by U_x/U_∞ (lower halves). Inside the separated region, two major recirculations are observed near the base and axis. With increased mass bleed, the axial directivity of the bleed jet becomes stronger, leading to a more intense secondary recirculation (near the base) and a weaker primary recirculation (near the axis). These flow characteristics can be apparently proved by checking the axial velocity contours. The primary recirculation moves downstream as I increases and, consequently, at $I = 0.0226$, it is observed to be negligible. Although both results are in qualitative agreement and the present computation offers proper predictions of the flowfields near the base, in which a relatively small separation bubble exists, it can be observed that there is a large discrepancy between the measured and computed primary recirculation lengths, which are specified by the forward S_f and rear S_r stagnation points. At $I = 0.0038$, the computed length is about 34% longer than the experimental length. In addition, significantly reduced recirculation in the measurement at $I = 0.0113$ is not reasonably simulated. This is mainly due to the inability of Reynolds-averaged Navier–Stokes (RANS) computations with turbulence models based on favorable pressure gradients

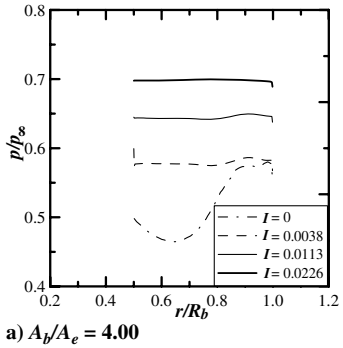

a) A_b/A_e = 4.00

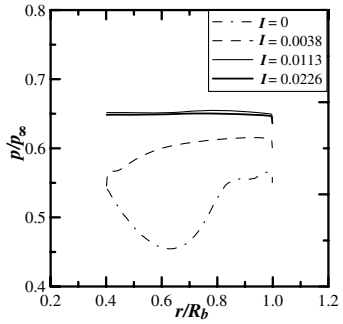

b) A_b/A_e = 6.25

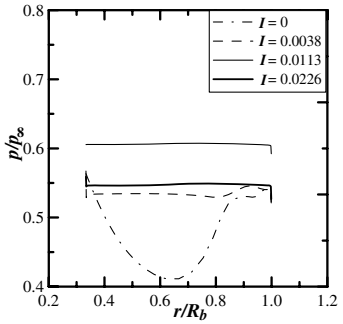

c) A_b/A_e = 9.00

Fig. 9 Base-pressure distributions with a change in I (R_e = 12.7 mm).

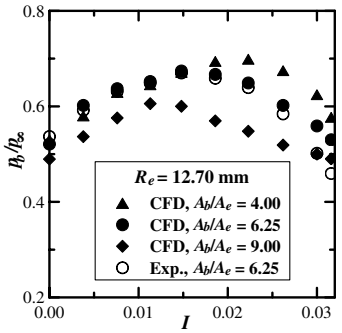

Fig. 10 Area-averaged base pressure vs I ($R_e = 12.7$ mm).

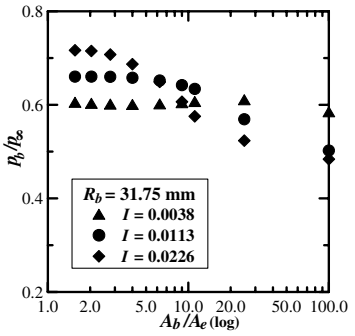

Fig. 12 Area-averaged base pressure vs A_b/A_e ($R_b = 31.75$ mm).

to correctly predict flowfields including large separation bubbles. The use of the axisymmetric solver rather than a full three-dimensional computation might add extra inaccuracy to the prediction of such a large-scale vortical flow.

Figure 9 shows base-pressure distributions for each base configuration tested with a change in the injection parameter. These results are presented for a fixed orifice diameter of 25.4 mm. Pressure values estimated along the base are nondimensionalized by the freestream pressure p_∞. Without base bleed in common, a large pressure gradient is existent and a very low-pressure region is formed around $r/R_b = 0.65$, due to a strong recirculating flow along the base, as observed in Fig. 6a. As I increases, however, such a gradient becomes smaller with an increased pressure level. When I reaches a certain value, the base-pressure level rather decreases, because the recirculation behind the base turns strong again, as shown in Fig. 8c. With an increased area ratio, this flow behavior is found at a relatively smaller I. It is also interesting to note that for a given injection parameter, the base-pressure level is higher at a smaller area ratio.

In Fig. 10, base-pressure values obtained through the present CFD analysis and an experiment [10] are given for all I values tested at $R_e = 12.7$ mm. The mean base pressure shown in the figure is obtained by the production of the base area and the resulting pressure force calculated through the area integral of base-pressure values. For all afterbody configurations considered, as I increases, base pressure rises up to a maximum value and then decreases. The present computations properly predict the experimental result that the maximum base pressure, leading to minimum base drag, for $A_b/A_e = 6.25$ is obtained at $I = 0.0148$. In the case of a larger area ratio, this optimum condition occurs at relatively smaller I, and the maximum base pressure that can be achieved by the use of mass bleed is lower. From the results discussed in this paper, it is considered that an increase and decrease in base pressure, such as changing mass bleed, is dependent mainly on the flow structure characterized by the recirculation regions deformed against I, and base drag can be more effectively controlled using smaller A_b/A_e.

The influence of the orifice exit area on the base flow is examined for each injection parameter. The base-pressure distributions shown in Fig. 11 were predicted for a single afterbody radius of 31.75 mm, and it thus means that the mass flow rate of the bleed jet is fixed for a given I value. Because a smaller orifice exit is used at a small value of I (Fig. 11a), the pressure distribution is obtained in a more uniform shape due to increased mass flux, but a change in pressure level is insignificant. In the same situation with relatively far stronger mass bleed (Fig. 11b), however, the pressure level decreases noticeably under similar flow characteristics, as shown in Fig. 8c.

For an injection parameter at $R_b = 31.75$ mm, Fig. 12 shows area-averaged base-pressure values obtained as the orifice exit area changes. As A_b/A_e increases (a decrease in orifice exit area), base pressure becomes lower from a certain area ratio, so far as mass bleed is not too weak (e.g., $I = 0.0038$). In this situation, for larger I, the feature occurs at a smaller area ratio with higher p_b. It should also be noticed that because A_b/A_e is larger than about 10, increasing I results in an adverse effect for base-drag reduction. These facts imply that an optimum area ratio exits, and the use of a larger orifice exit can give a wider range of base-drag control.

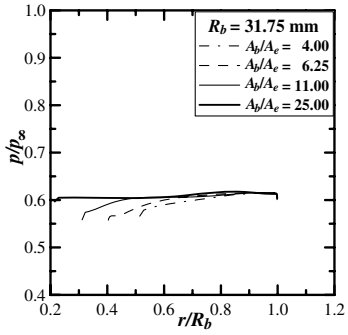

a) I = 0.0038

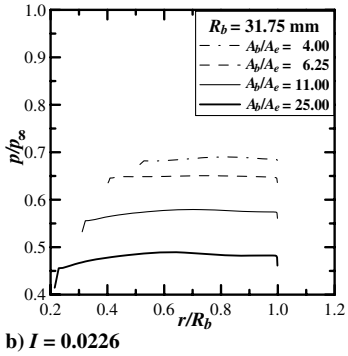

b) I = 0.0226

Fig. 11 Base-pressure distributions with a change in I ($R_b = 31.75$ mm).

Conclusions

A Mach 2.47 base flow was investigated to understand the effects of mass bleed on base flow characteristics and base pressure for various base-to-orifice-exit area ratios, conducting a numerical analysis. Axisymmetric, compressible, mass-averaged Navier–Stokes equations were computed using the standard k-ω model, a fully implicit finite volume scheme, and a second-order upwind scheme. The injection parameter and area ratio were changed to provide various characteristics of base flows with a subsonic bleed jet issued into the wake region downstream of the afterbody base.

The present computation showed that strongly recirculating flows formed near the base and model axis were weakened considerably by the use of an appropriate amount of mass bleed. A change in the mass flow rate of the bleed jet led to a significant variation of the flow structure in the separation region behind the base. As the injection parameter increased over a certain value, base flow turned to a similar pattern in structure. For all afterbody configurations tested, during the augmentation of mass bleed, the average base pressure reached a maximum value at a particular injection parameter, which is considered as an optimum control condition. For either a smaller base or larger orifice exit, the optimum condition leading to minimum base drag occurred at relatively stronger mass bleed, and such a base configuration could offer a larger control threshold. Under a constant injection parameter, base pressure became lower over a certain area

ratio. When the orifice exit was too small (A_b/A_e greater than about 10), an increase in I gave an adverse effect on base-drag reduction. For achieving required control performance, therefore, the mass flow rate of the bleed jet and base-orifice design should be carefully considered together.

References

[1] Sahu, J., and Nietubicz, C. J., "Navier–Stokes Computations of Projectile Base Flow with and Without Mass Injection," *AIAA Journal*, Vol. 23, No. 9, 1985, pp. 1348–1355.

[2] Viswanath, P. R., and Patil, S. R., "Effectiveness of Passive Devices for Axisymmetric Base Drag Reduction at Mach 2," *Journal of Spacecraft and Rockets*, Vol. 27, No. 3, 1990, pp. 234–237.

[3] Wood, C. J., "Visualisation of an Incompressible Wake with Base Bleed," *Journal of Fluid Mechanics*, Vol. 29, No. 2, 1967, pp. 259–272.

[4] Murthy, S. N. B., and Osborn, J. R., "Base Combustion Effects on Base Pressure," *Aerodynamics of Base Combustion*, Progress in Astronautics and Aeronautics, Vol. 40, AIAA, New York, 1976, pp. 307–338.

[5] Nash, J. F., Quincey, V. G., and Callinan, J., "Experiments on Two-Dimensional Base Flow at Subsonic and Transonic Speeds," Reports and Memoranda, Aeronautical Research Council Rept.. 3427, 1966.

[6] Addy, A. L., "Thrust-Minus-Drag Optimization by Base Bleed and/or Boattailing," *Journal of Spacecraft and Rockets*, Vol. 7, No. 11, 1970, pp. 1360–1362.

[7] Bowman, J. E., and Clayden, W. A., "Cylindrical Afterbodies in Supersonic Flow with Gas Ejection," *AIAA Journal*, Vol. 5, No. 8, 1967, pp. 1524–1525.

[8] Bourdon, C. J., and Dutton, J. C., "Visualization of a Central Bleed Jet in an Axisymmetric, Compressible Base Flow," *Physics of Fluids*, Vol. 15, No. 2, 2003, pp. 499–510.

[9] Wilcox, D. C., *Turbulence Modeling for CFD*, DCW Industries, Inc., La Canada, CA, 1998.

[10] Mathur, T., and Dutton, J. C., "Velocity and Turbulence Measurements in a Supersonic Base Flow with Mass Bleed," *AIAA Journal*, Vol. 34, No. 6, 1996, pp. 1153–1159.

[11] Herrin, J. L., and Dutton, J. C., "Supersonic Base Flow Experiments in the Near Wake of a Cylindrical Afterbody," *AIAA Journal*, Vol. 32, No. 1, 1994, pp. 77–83.

[12] *FLUENT 6 User's Guide*, Vol. 2, Fluent Inc., Lebanon, NH, 2003.

[13] Venkateswaran, S., Weiss, J. M., and Merkle, C. L., "Propulsion Related Flowfields Using the Preconditioned Navier–Stokes Equations," AIAA Paper 92-3437, July 1992.

[14] Lee, Y. K., Raghunathan, S., and Benard, E., "Passive Control of Plume Interference on Axisymmetric Slender Bodies," *AIAA Journal*, Vol. 43, No. 8, 2005, pp. 1653–1662.

[15] Barth, T. J., and Jespersen, D., "The Design and Application of Upwind Schemes on Unstructured Meshes," AIAA Paper 89-0366, 1989.

[16] Jameson, A., Schmidt, W., and Turkel, E., "Numerical Solution of the Euler Equations by Finite Volume Methods Using Runge-Kutta Time-Stepping Schemes," AIAA Paper 81-1259, 1981.

[17] Wilcox, D. C., "Turbulence and Transition Modeling for High-Speed Flows," NASA CR-191473, 1993.

G. Candler
Associate Editor